

Article

Magmatic Intrusion during the Yanshanian Period and Multi-Mineral Enrichment Mechanisms in the Eastern Margin of the North China Craton

Lusheng Yin ^{1,2}, Huaihong Wang ³, Dongdong Wang ^{2,*}, Yinan Liu ², Haiyan Liu ², Yuzhen Zhu ⁴, Lijun Shen ⁴ and Zengxue Li ²

¹ College of Geoscience and Surveying Engineering, China University of Mining and Technology, Beijing 100083, China; yinlusheng_8@126.com

² College of Earth Science and Engineering, Shandong University of Science and Technology, Qingdao 266590, China; lizengxue@126.com (Z.L.)

³ Shandong Coal Geology Bureau, Jinan 250104, China

⁴ Geological Planning and Exploration Institute of Shandong Coalfield, Jinan 250104, China; zhuyuzhen2008@163.com (Y.Z.); sdmts1j@163.com (L.S.)

* Correspondence: wdd02_1@163.com

Abstract: The mineralization within the North China Craton (NCC) is intricately linked to Mesozoic large-scale extension in eastern China and is a consequence of a unified geodynamic tectonic background. Despite previous attempts to elucidate the relationship between large-scale mineralization and magmatic activity in the NCC, a lack of systematic research has hindered the identification of connections among deposits with inconsistent metallogenic ages. This study focuses on the coal measures of the Huanghebei Coalfield (HHBC) in western Shandong, presenting a regional magmatic–hydrothermal metallogenic system with a genetic connection. It delves into the intricate interplay between the multi-mineral enrichment mechanism, metallogenic regularity, and the NCC’s destruction. The findings reveal that: (1) Various stages of magmatic intrusion during the Yanshanian period significantly influenced the Late Paleozoic coal measures in the HHBC. The coal measures exhibit distinct ranks, ranging from medium-rank bituminous C to A and high-rank anthracite C, resulting in noticeable differences in gas generation among different coal ranks. The shale between the coal seams C5 and C7 emerges as excellent with a good hydrocarbon-generating capacity during the middle-maturity stage. (2) The “Intrusion along the rock layer type” proves most conducive to shale gas enrichment, while the “laccolith type” is more favorable for shale gas enrichment compared to “dike type” intrusions, which have a limited impact on shale gas enrichment. (3) The mineralization process of CBM, shale gas, and iron ore is influenced by Yanshanian-period magma. The enrichment degree of CBM and shale gas exhibits an inverse correlation with the distance from the magmatic intrusion. Iron deposits demonstrate a close association with the magmatic intrusion, with enhanced enrichment along the rock layer. The results indicate that the destruction of the NCC triggered intense metasomatism in the deep cratonic fluids, serving as the primary driving mechanism for large-scale mineralization during the Yanshanian period. Magmatic intrusions bring hydrothermal fluids conducive to mineralization, and the heat release from these intrusions promotes thermal evolution, hydrocarbon generation, and the enrichment of organic-rich strata.



Citation: Yin, L.; Wang, H.; Wang, D.; Liu, Y.; Liu, H.; Zhu, Y.; Shen, L.; Li, Z. Magmatic Intrusion during the Yanshanian Period and Multi-Mineral Enrichment Mechanisms in the Eastern Margin of the North China Craton. *Minerals* **2024**, *14*, 332. <https://doi.org/10.3390/min14040332>

Academic Editor: Giovanna Rizzo

Received: 11 February 2024

Revised: 15 March 2024

Accepted: 22 March 2024

Published: 24 March 2024



Copyright: © 2024 by the authors. Licensee MDPI, Basel, Switzerland. This article is an open access article distributed under the terms and conditions of the Creative Commons Attribution (CC BY) license (<https://creativecommons.org/licenses/by/4.0/>).

Keywords: Yanshanian period; skarn-type iron ore; CBM; shale gas; magmatic–hydrothermal metallogenic system; NCC

1. Introduction

The North China Craton (NCC for short) is the main tectonic unit of the Chinese mainland, covering an expansive area of approximately 1.3×10^6 km² and boasting an ancient history of 3.8 billion years [1]. During the Mesozoic, significant craton destruction

and lithospheric thinning unfolded within the NCC [2]. The focal point of craton destruction was primarily in the eastern part, reaching its zenith around 125 Ma, while the western part underwent a notable transformation of the craton [3]. The primary external factor and driving force behind the NCC's destruction during the Early Cretaceous was the subduction of the western Pacific plate beneath the Eurasian plate [4]. The retention and dehydration of the subducted plate in the mantle transition zone induced melting and unsteady flow in the overlying mantle. Additionally, the retreat of the subduction zone triggered robust lithospheric extension, ultimately leading to the NCC's destruction [2,3,5]. This process played a pivotal role in the formation of oil and gas-bearing basins, as well as the development of large-scale metal mineral resources in eastern China [6].

Against the tectonic backdrop of the NCC's destruction, the western Shandong Province (Luxi) area witnessed the emergence of large-scale magmatic activity, extensive basin depression, and rapid crustal uplift. Concurrent with the craton's destruction, significant mineralization unfolded along the eastern margin of the NCC [6]. This mineralization encompasses various resources such as CBM, shale gas, tight gas, and iron ore. Notably, skarn iron ore stands out as a vital source of high-grade iron ore in China [7]. The eastern regions of Daye, Linfen, and Laiwu are particularly rich in skarn iron deposits, boasting the highest concentration in China. Dominated by magnetite, skarn iron ore results from hydrothermal metasomatism between magma–hydrothermal fluid and Paleozoic or early Mesozoic marine carbonate rocks [8–10]. The primary resources within the oil and gas-bearing basin consist mainly of CBM and shale gas, both of which are found in the Carboniferous–Permian coal measures. Recent research data on multi-mineral resources indicate a correlation between their formation and Early Cretaceous magmatic intrusion [11]. While current studies focus on the geochemistry and chronology of skarn-type iron ore [12] and the magmatic intrusion and Paleozoic multi-mineral metallogenic mechanism [11], there has been limited exploration into the genetic relationship and enrichment mechanism between these deposits. The question of whether these deposits of varying ages collectively form a magma–hydrothermal metallogenic system with a regional genetic connection is a topic worthy of further discussion [13].

This study delved into the HHBC in the eastern margin of the NCC and provided a comprehensive analysis of the relationship between geochemical changes caused by the magmatic intrusion on coal measures strata and hydrocarbon generation potential of source rocks, as well as the influence of the ore body mineralization mechanism. This study proposed a regional magma–hydrothermal metallogenic system with genetic links and investigated the connection between the multi-mineral enrichment mechanism, mineralization regularity, and the destruction of the NCC.

2. Geological Background

2.1. Tectonic Setting

The NCC is located in the northeastern margin of the Paleo–Tethys Ocean (Figure 1a), spanning a latitude of approximately 10–20° N [14,15]. It is surrounded by the Central Asian Orogenic Belt to the north and the Central China Orogenic Belt to the south. The western boundary is the Qilian Orogenic Belt, and the eastern boundary is the Sulu Orogenic Belt [16]. The NCC is divided into three parts from west to east: the Western Block, the Central Zone, and the Eastern Block. The HHBC is located in the Eastern Block, east of the NCC, exhibiting similar phased evolution characteristics as the NCC (Figure 1c). It extends from the Woniushan Fault in the east to the Liuji Fault in the west, with the coal measure bottom outcrop in the south and the Qiguang Fault in the north [17]. The strata in the area, from old to new, include the NeoArchean Taishan Group, Cambrian, Ordovician, Carboniferous, Permian, Triassic, Paleogene, Neogene, and Quaternary. The Carboniferous Permian is an important coal measure that successively consists of the Benxi Formation, Taiyuan Formation, Shanxi Formation, Lower Shihezi Formation, and Upper Shihezi Formation. Due to the long-term block uplift in the middle Shandong Province, the regional strata in the HHBC generally display a noticeable gentle monoclinical structure.

The strata strike N 50° E, with a dip direction of N 40° W and a dip angle ranging from 5° to 8° [18] (Figure 1d).

2.2. Characteristics and Spatial Distribution of Magmatic Intrusions

Against the tectonic backdrop of the North China Craton's (NCC) destruction, extensive magmatic activity unfolded in the western Shandong area. This activity primarily comprised the Middle Jurassic and Early Cretaceous magmatic events. The Middle Jurassic magmatic activity had a limited distribution range, while the Early Cretaceous magmatic activity was more intense and widely distributed. Throughout its intrusion process, it underwent varying degrees of separation crystallization, magma mixing, and crustal contamination, resulting in the formation of various intermediate-acidic intrusive rocks in the shallow crust [19–22]. Common magmatic intrusions occurred in the Carboniferous–Permian coal measures and Ordovician limestone. During this period, the intrusions mainly developed in three layers, with acidic granite in the upper and lower layers and intermediate-basic diorite in the middle layer [23] (Figure 1d).

In the study area, acidic rocks are mainly distributed in the Qihe–Yucheng area, existing within the Carboniferous–Permian coal measures in the form of rock beds. They exhibit a widespread distribution in the western and southeastern parts of the study area. The coal measures of the Carboniferous–Permian Shanxi and Taiyuan Formations generally experience magma intrusion. The magma permeates along the rock formations or coal seams, running parallel to the surrounding rock and forming tabular intrusion bodies, rock beds, and rock loccoliths. The thickness of the upper and lower layers of acidic intrusions varies significantly. The upper intrusion layers are primarily associated with strata above the roof of No. 3 and No. 4 coal seams (C3 and C4) in the lower member of the Shanxi Formation. The magmatic rocks gradually thin and pinch in the southwest and northeast directions. The middle layer basic intrusion exhibits minimal thickness variation, with the intrusion layer affecting the No. 5 to No. 9 coal seams (C5 to C9) of the middle and upper members of the Taiyuan Formation. This intrusion layer significantly impacts the No. 7 coal seam and connects with the Ji'nan gabbro rock mass to the east. The lower intrusion beds are mainly associated with the No. 11 and No. 13 coal seams (C11 and C13) of the Taiyuan Formation, gradually pinching out to the southwest.

The intermediate-basic rock mass mainly lies beneath the surface in the Litun, Pandian, and Dazhang areas, primarily consisting of diorite in terms of lithology (Figure 1d). Its diagenetic age closely aligns with the rocks of the Ji'nan sequence, and it is considered to be a component of the Ji'nan sequence. Magma intrusion predominantly occurs in the form of a batholith, with instances of rock veins or rock wall intrusions along the structural fracture. Within this sequence, the basic magmatic rocks demonstrate a significant association with the magnetite mineralization in the Qihe–Yucheng region. The intermediate-basic magmas intruded into the Mesozoic coal measures during the Late Yanshanian period. The boundary of the rock mass and the contact zone between the Ordovician and Carboniferous–Permian formations represents favorable locations for iron ore mineralization.

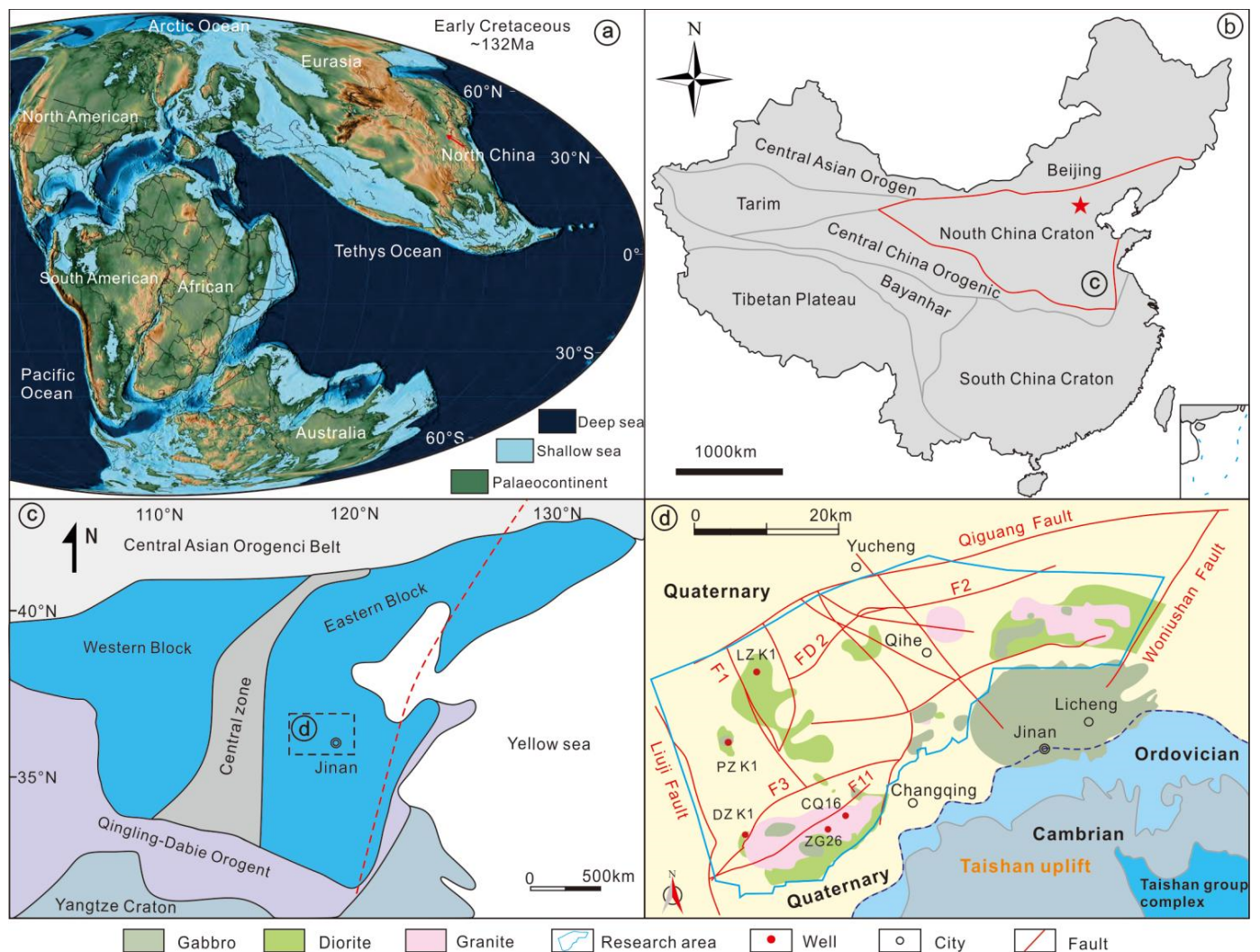


Figure 1. Location and geological context for the HHBC. (a) Paleogeographic map of Early Cretaceous NCC [24]. (b) Map of China showing the boundary of NCC (<http://bzdt.ch.mnr.gov.cn/>, accessed on 11 February 2023, No. GS (2016)1569). (c) A simplified map showing the tectonic divisions of the NCC and adjacent regions [25,26]. (d) Tectonic geological setting for the HHBC [23].

2.3. Characteristics and Spatial Distribution of Skarn-Type Iron Ores

Skarn-type iron ore deposits are an important type of deposit in the HHBC. They are formed by hydrothermal metasomatism in or near the contact zone between medium acid and medium basic intrusive rocks and carbonate rocks. Among them, skarn mainly refers to calcisilicate rock and skarn iron ore as containing iron oxide, such as magnetite or hematite. The primary source of ore-forming materials of skarn-type iron ore deposits in the HHBC is the intrusion of the magmatic rock, specifically diorite. Within the diorite body, various dyke intrusions such as gabbro, diorite porphyry, monzonite porphyry, and diabase exist, broadly categorized into basic and intermediate-acidic dykes. The distribution of iron ore bodies is diverse and intricately linked to the contact relationship between diorite bodies and carbonate strata. The ore-forming geological body of the HHBC is dominated by diorite and gabbro, and there are diorite porphyrite, monzonite porphyry, diabase, and other dike intrusions. Diorite is gray and has a granular and massive structure. Its main minerals include plagioclase, hornblende, biotite, potassium feldspar, quartz, and so on. Local rock alterations and metasomatism are more obvious. Gabbro is often located between the diorite and skarn belt or in the diorite rock mass. Its fresh surface is grain-green, and it has a massive, medium-fine grain granular structure. Its main minerals include plagioclase,

pyroxene, a small amount of potassium feldspar, and biotite, while its secondary minerals include sphalerite, apatite, ilmenite, magnetite, and so on.

Based on the contact relationship between the iron ore body and surrounding rock, three types of metallogenic structural plane styles are identified as follows: (1) Contact zone structure: This structure predominates in the contact zone between the ore-forming geological body and limestone, representing a crucial structural plane in the contact metamorphic iron ore within the study area. (2) Interlayer structure: Ore bodies are primarily formed in layers along veins. (3) Fault zone structure: The ore body is generated within the fault structure. These structural styles provide insights into the diverse modes of iron ore formation within the HHBC, emphasizing the importance of the contact relationship between geological bodies and surrounding strata.

3. Thermal Evolution and Gas Enrichment Mechanism of Source Rocks

3.1. Metamorphism of Coal Seam and Enrichment Mechanism CBM

The superimposed position of the three-layer magmatic intrusion in the HHBC is located in the Changqing Wellfield in the southeast of the study area. The thickness, area, and intrusion horizon of the magmatic rock intrusions surpass those in the adjacent area. The three-layer intrusive rock bed is predominantly formed in the coal measures of the Shanxi Formation and the Taiyuan Formation, exhibiting strong activity. The intensity and extent of magmatic rock intrusion into each coal seam in the Changqing Wellfield varies, resulting in differences in coal metamorphism degrees. The coalification of organic matter in coal in geological history, that is, coal rank or thermal maturity, is usually measured by vitrinite reflectance, based on the "Data Measurement Method of Vitrinite Reflectance of Sedimentary Rocks" (SY/T 5124-1995) [23]. The maximum vitrinite reflectance (R_{\max}^0 , %) of coal and rock in the Changqing Wellfield ranges from 0.81% to 3.20% (Figure 2). The variation in R_{\max}^0 , % within each coal seam reflects the difference in coal rank and change in gas generation capacity, with coal rank classified according to ISO 11760-2005 "International Standard for Coal Classification" [27]. It is divided into low-rank (R_{\max}^0 , % < 0.5%, lignite, sub-bituminous), mid-rank ($0.5\% < R_{\max}^0$, % < 2.0%, bituminous), and high-rank coal (R_{\max}^0 , % > 2.0%, anthracite).

Among them, the metamorphic degree of C5 is relatively low in each exploration area, with R_{\max}^0 , % ranging from 0.59% to 2.26% (average 1.53%). It primarily consists of medium-rank bituminous C to bituminous A, and high-rank anthracite C (Figure 2a). The gas content of C5 is notably higher at 6.32 m³/t compared to other coal seams, making it a favorable layer for gas generation (Table 1). For C7, R_{\max}^0 , % ranges from 0.75% to 0.96% (average 0.82%) and is mainly composed of medium-rank bituminous C (Figure 2b). The gas content of C7 is 4.66 m³/t (Table 1). C10 exhibits R_{\max}^0 , % ranging from 0.74% to 0.97% (average 0.81%), primarily composed of medium-rank bituminous C (Figure 2c). The gas content of C10 is 5.01 m³/t (Table 1). C11 displays R_{\max}^0 , % ranging from 0.72% to 6.35% (average 3.20%), consisting mainly of medium-rank bituminous C to bituminous A and high-rank anthracite C to anthracite A, (Figure 2d). The gas content of C11 is 3.28 m³/t (Table 1). C13 has R_{\max}^0 , % ranging from 0.70% to 2.38% (average 0.92%), mainly comprising medium-rank bituminous C to bituminous A and high-rank anthracite C (Figure 2e). The gas content of C13 is 2.43 m³/t (Table 1).

The planar distribution of coal in C5, C7, and C10 (upper coal group) in the Changqing Wellfield indicates that coal in the high metamorphic stage is mainly distributed in the middle and deep sections of the mine, aligning closely with the distribution range of three layers of magmatic rocks (Figures 1d and 2a–c). The planar distribution of coal types in C11 and C13 (lower coal group) in the Changqing Wellfield reveals that the range of magmatic rock essentially corresponds to the variations in coal metamorphism degree (Figures 1d and 2d,e). Originating from the magmatic rock intrusion site, it transitions from natural coke to bituminous towards the surrounding coal metamorphism stages. This demonstrates that the magmatic intrusion has a direct impact on coal, showcasing changes in coal types [28]. Additionally, it illustrates that the coal seam in high coal-rank areas is

often regarded as a better gas target horizon. Based on the measured data of Changqing Wellfield's gas content, there is a notable disparity in CBM content between the upper and the lower coal groups. The gas content of the upper coal group is high, while the gas content of the lower coal group is generally low.

Table 1. The R^0_{max} , %, coal thickness, gas content, and metamorphism stage of a coal seam in HHBC (data from the Geological Planning and Exploration Institute of Shandong Coalfield, 2020).

Changqing Wellfield	C5	C7	C10	C11	C13
R^0_{max} , %	0.79~2.26 $\bar{X} = 1.53$	0.75~0.96 $\bar{X} = 0.82$	0.74~0.97 $\bar{X} = 0.81$	0.72~6.35 $\bar{X} = 3.20$	0.70~2.38 $\bar{X} = 0.92$
coal rank	bituminous C–A, anthracite C	bituminous C	bituminous C	bituminous C–A, anthracite C–A	bituminous C–A, anthracite C
metamorphism stage	high maturity stage	maturity stage	maturity stage	over maturity stage	high maturity stage
coal thickness (m)	0~0.90 $\bar{X} = 0.69$	0.34~1.01 $\bar{X} = 0.82$	0.35~1.35 $\bar{X} = 0.80$	0~4.10 $\bar{X} = 1.58$	0.75~3.30 $\bar{X} = 1.92$
gas content (m^3/t)	0.05~15.28 $\bar{X} = 6.32$	0.01~7.31 $\bar{X} = 4.66$	4.51~5.51 $\bar{X} = 5.01$	1.20~5.37 $\bar{X} = 3.28$	0.04~5.44 $\bar{X} = 2.43$

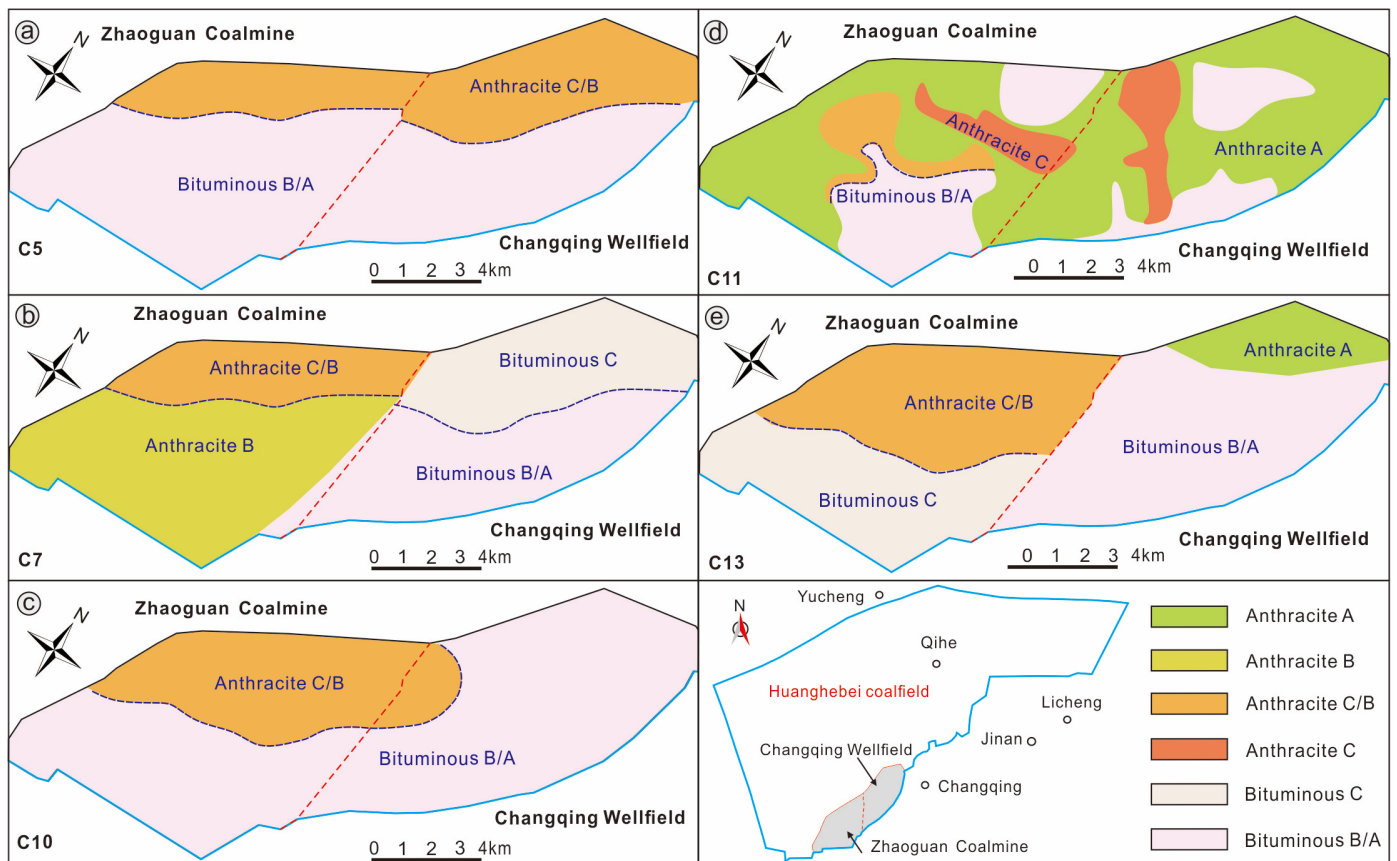


Figure 2. Characteristics of coal types in the southeast of the HHBC of Carboniferous–Permian. (a–e) is the C5, C7, C10, C11, C13 coal-type characteristics of Zhaoguan and Changqing Wellfield.

Under normal circumstances, it is generally observed that the greater the burial depth of the coal seam, the higher the gas content [29]. However, the opposite holds true for CBM content in the Changqing Wellfield. Previous studies suggest that reservoir structure serves as the most crucial and direct factor influencing gas content [30,31]. On the one hand, it directly or indirectly governs the distribution, migration, accumulation, and formation of coal seams and CBM. On the other hand, it induces constructive or destructive changes in the existing CBM formation [32]. Coal reservoirs with different tectonic types exhibit distinct methane adsorption characteristics, potentially leading to variations in CBM enrichment conditions [33–36]. Examining the sedimentary evolution and regional tectonic evolution characteristics of coal seams in the HHBC, both the upper and lower coal seams belong to the Taiyuan Formation, sharing similar evolution traits. Furthermore, prior research has demonstrated that the sealing conditions of surrounding rock and regional hydrogeological characteristics influence the generation, migration, and enrichment of CBM [30,37,38]. However, these factors are not the primary controlling factors for the abnormal characteristics of CBM content in the study area.

Based on the aforementioned studies, it is asserted that the manner and extent of magma intrusion into coal seams, coupled with the adsorption characteristics of coal at different metamorphic degrees, are the primary factors contributing to the generally lower CBM content in the lower coal group is generally lower compared to the upper coal group. Magmatic intrusions are predominantly concentrated in the western and southeastern parts of the HHBC, leading to the thermal metamorphism and contact metamorphism of coal measures, resulting in an increased degree of coal metamorphism [39]. In the study area, coal metamorphism is chiefly manifested as magmatic thermal contact metamorphism. This metamorphism occurs due to the intrusion of magma passing through or near the coal seam. The thermal energy from these intrusions induces metamorphism in the coal seam at temperatures exceeding 1000 °C, playing a pivotal role in the thermal maturation of organic matter [40,41]. Under the influence of high temperatures, the coal seam generates secondary gas, leading to a sharp increase in CBM content, elevating coal reservoir pressure, and forming abnormal high pressure. This abnormally high pressure facilitates the creation of numerous micro-cracks in coal seams, roofs, and floors, forming effective migration channels. Simultaneously, it prompts the diffusion and migration of CBM to low-pressure areas [42,43]. Furthermore, magmatic intrusion often disrupts the integrity of surrounding rock and coal seams, resulting in the formation of fracture channels. A significant volume of gases generated within the coal seams, along with a considerable amount of volatiles carried by the magma itself, escapes through these fracture channels.

3.2. Shale Thermal Evolution Degree and Shale Gas Enrichment Mechanism

The maturity of source rocks refers to the degree of thermal evolution experienced by source rocks in the geological history, and is an important index to evaluate whether source rocks have hydrocarbon generation ability. The maturity of organic matter of source rocks can be measured by means of petrology, geochemistry, geophysics, R_{\max}° , palynology, and other indicators [44]. This study mainly focuses on R_{\max}° and rock-eval, which is used to reflect the gas generation degree of carbonaceous mudstone in HHBC, and according to the People's Republic of China Coal Industry Standard Catalog (2010), the classification of coal grades is made. At the same time, according to the "Regulation of shale gas resources/reserves estimation" (DZ/T 0254-2014), the degree of thermal evolution of shale gas layers is classified.

The test results of shale samples from well CQ16 in the study area indicate that the pyrolysis peak temperature (T_{\max} , °C) of dark shale ranges from 471.9 °C to 476.4 °C (Table 2), and the T_{\max} begins to rise in the S5 layer, but the shale mostly remains in the middle mature stage during the entire period. The values of S_1 and S_2 exhibit significant variations in different shale formations, leading to considerable heterogeneity in hydrocarbon generation potential. The highest value of $S_1 + S_2$ can reach 17 mg/g, with the peak value occurring in the S11 layer between C5 and C7, representing a promising hydrocarbon

source rock (Figure 3). In the study area, R^0_{max} ranges from 0.72% to 1.25%, and its thermal evolution degree distribution aligns closely with the range of the three-layer magmatic rocks (Figure 4). The upper magma is primarily distributed in the southwest region of the study area, with R^0_{max} mostly falling between 0.7% and 0.9%. The thermal evolution degree gradually increases to the north around the rock mass. The middle constitutes a basic intrusion rock with a wide range of magmatic intrusion and a high thermal evolution degree. R^0_{max} is predominantly between 1.0% and 1.2%, reaching more than 1.2% in local areas. Around the invasion site, the thermal evolution degree of shale is noticeably reduced, indicating a discernible pattern. The lower layer magmatic rocks are less distributed, and the thermal evolution around the intrusions is higher.

Table 2. Shale thermal evolution degree in HHBC of Permian–Carboniferous.

Sample No.	Depth (m)	Tmax (°C)	Maturity	S1 (mg/g)	S2 (mg/g)	S1 + S2 (mg/g)	Source Rock Rank
S1	526.84	471.9	moderate	0.05	0.73	0.78	poor
S2	545.03	471.9	moderate	0.01	0.18	0.19	no
S3	555.32	471.9	moderate	0.01	0.08	0.09	no
S4	657.2	471.9	moderate	0.01	0.10	0.12	no
S5	660.51	476.4	moderate	0.04	0.09	0.13	no
S6	668	476.4	moderate	0.02	0.09	0.10	no
S7	682.39	476.4	moderate	0.12	0.33	0.45	no
S8	692.25	476.4	moderate	0.27	0.93	1.20	poor
S9	699.83	476.4	moderate	0.25	0.84	1.09	poor
S10	702.07	476.4	moderate	0.12	0.58	0.70	poor
S11	707.37	476.4	moderate	2.95	14.50	17.45	good
S12	709.6	476.4	moderate	0.38	1.73	2.10	medium
S13	711.25	476.4	moderate	0.76	12.53	13.29	good
S14	721.71	476.4	moderate	0.08	0.67	0.75	poor
S15	725.53	476.4	moderate	0.09	0.83	0.93	poor
S16	740.33	476.4	moderate	0.11	1.41	1.52	poor
S17	742.79	476.4	moderate	0.09	1.11	1.20	poor
S18	752.22	476.4	moderate	0.13	1.39	1.51	poor
S19	755.8	476.4	moderate	0.17	1.54	1.71	poor
S20	757.5	476.4	moderate	0.08	0.24	0.32	no
S21	766	476.4	moderate	0.10	0.20	0.30	no
S22	790.94	476.4	moderate	0.13	1.59	1.72	poor
S23	793.14	476.4	moderate	0.07	0.92	0.99	poor
S24	798.5	476.4	moderate	0.10	0.60	0.70	poor
S25	807.88	476.4	moderate	0.13	1.36	1.50	poor
S26	812.06	476.4	moderate	0.10	0.91	1.01	poor
S27	821.55	476.4	moderate	0.35	3.88	4.23	medium
S28	823.55	476.4	moderate	0.12	0.92	1.03	poor
S29	824	476.4	moderate	0.16	1.20	1.36	poor
S30	830.55	476.4	moderate	0.21	2.49	2.70	medium
S31	842.44	476.4	moderate	0.06	0.88	0.93	poor
S32	851.72	476.4	moderate	0.07	0.70	0.77	poor
S33	769.96	476.4	moderate	0.12	4.24	4.36	medium
S34	817.6	476.4	moderate	0.15	0.28	0.43	no

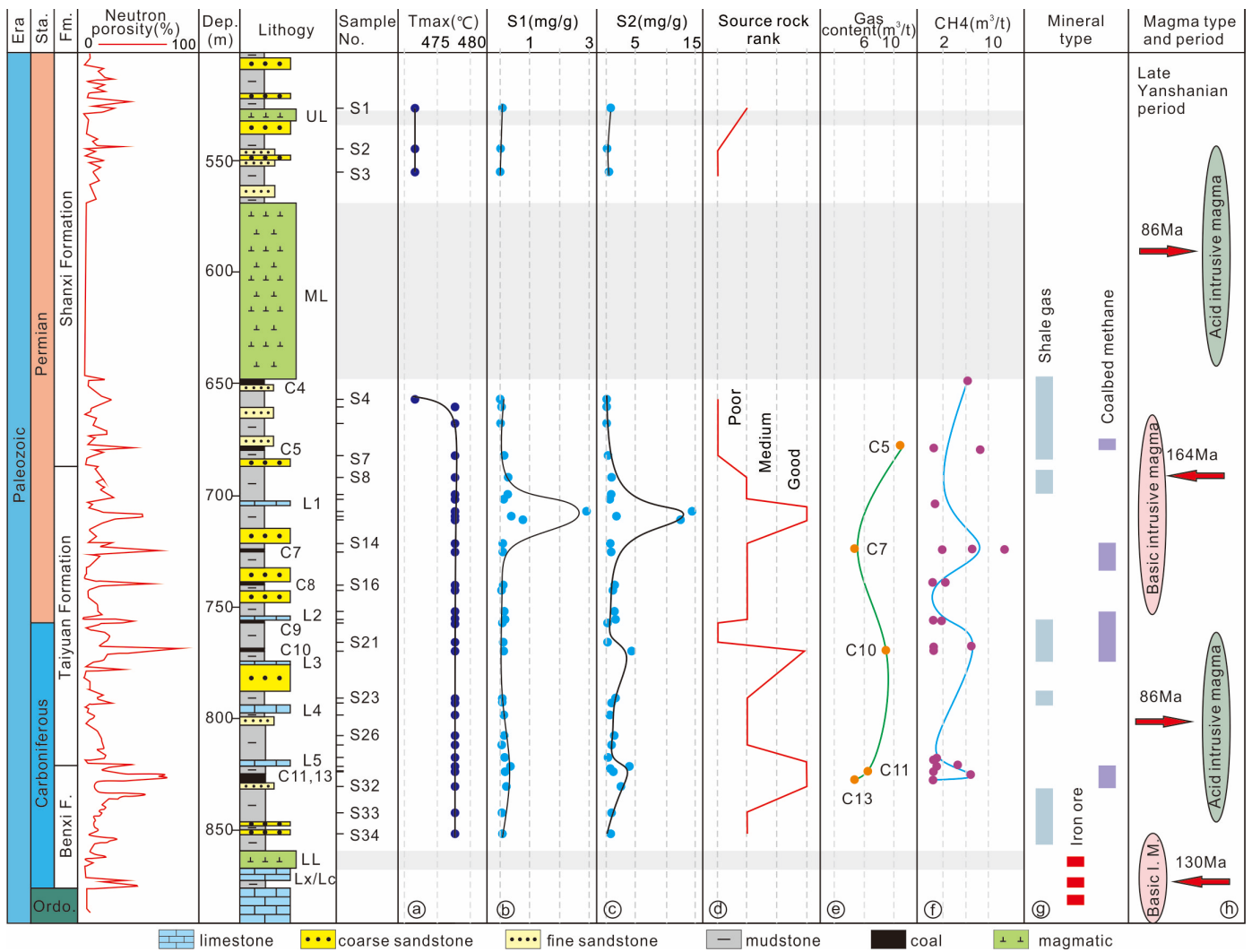


Figure 3. The analysis result of Well CQ16 Carboniferous–Permian coal measures, Tmax, S1, S2, Source rock rank, gas content, CH4, and magma type. (a–c) Tmax, S1, S2 vertical data evolution trend; (d) There are three types of Source rock rank; (e) The gas content and vertical characteristics of coal seam; (f) CH4 and vertical characteristics of shale; (g) Mineral type, include shale gas, coalbed methane, iron ore [23]; (h) The study area is a Basic intrusive magma, 130 Ma [23] 164 Ma, Acid intrusive magma, 86 Ma [7]. Abbreviations: Ordo = Ordovician, Sta. = Stage, Fm. = Formation, Dep. = Depth, Basin i. m. = Basin intrusion magma, C5 = No. 5 coal seam, L1 = No. 1 limestone, Lx = xujiazhuang limestone, Lc = caobugou limestone, LL = lower layer, ML = middle layer, UL = upper layer.

When magma infiltrates the shale layer, influenced by high temperature [45], high pressure (Das et al., 2014) [46], and hydrothermal fluid [47], it induces profound changes in the organic geochemical characteristics and physical properties of the shale reservoir. These alterations deviate significantly from those observed in the natural evolutionary context [48]. Such transformations have a direct impact on rock formation, pore evolution, and the enrichment of shale gas in the neighboring area of the intrusion. The high temperature brought about by magma plays a crucial role in the formation of solid bitumen [49,50] and contributes to the maturation of organic matter near the vicinity of the intrusion [49–53]. The R_{max}^o of shale in the magmatic rock development area in the middle of the study area significantly exceeds that in the surrounding areas, providing additional evidence of the magmatic intrusion’s influence on the maturity of shale organic matter. The magma intrusion also triggers an escalation in tectonic stress, fostering hydrocarbon generation,

increasing fracture density, enhancing reservoir performance, and augmenting shale adsorption capacity. In summary, the intrusion of magma instigates a complex interplay of geological and geochemical factors, reshaping the composition of shale and creating conditions conducive to the accumulation of shale gas in the adjacent area [54,55].

At the basin scale, shale can expedite hydrocarbon generation during magmatism, yielding a substantial amount of methane [56–58]. The impact of different magma occurrences varies in their effects on shale gas enrichment. In the study area, three models of magma intrusion into shale are identified. When magma intrudes along the rock layer, it induces extensive thermal metamorphism in the upper shale reservoir, leading to the rapid generation of methane from organic matter. Due to the shale reservoir’s significant gas storage capacity and the intrusion layer preventing the escape of shale gas, this scenario proves beneficial to shale gas enrichment (Figure 5b). In cases where intrusive magma follows a “laccolith type” intrusion into the shale layer, it results in a subdued thermal effect on the lower shale reservoir. The influence range of magmatic activity is limited, rendering the enrichment of shale gas neutral (Figure 5c). Contrarily, when intrusive magma follows a “dike type” intrusion into the shale layer, it creates a fracture channel at the contact area between the dikes and the reservoir. This channel facilitates the escape of shale gas and proves unfavorable to the enrichment of shale gas (Figure 5d).

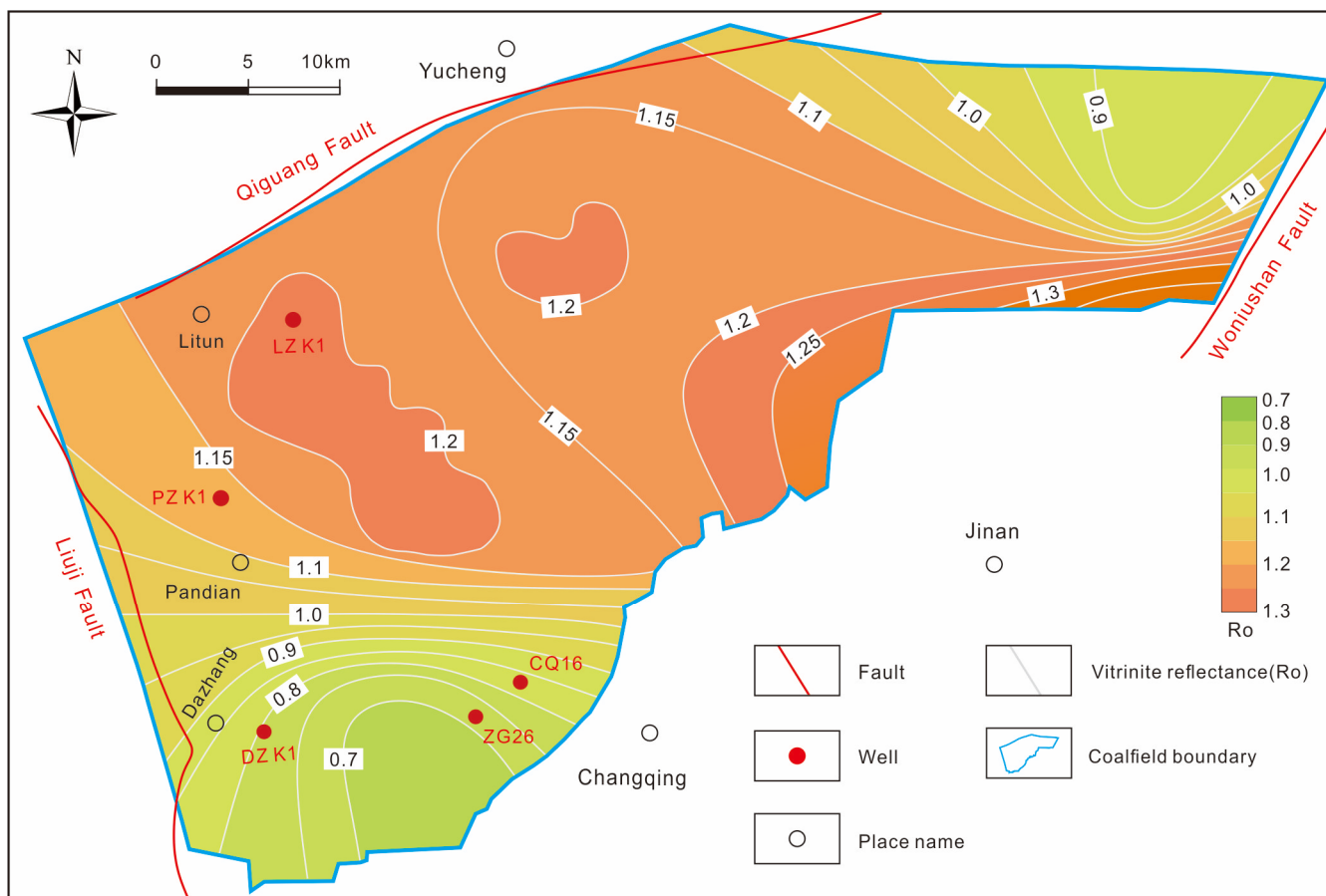


Figure 4. The distribution of R_{0max} , % in HHBC of Carboniferous–Permian.

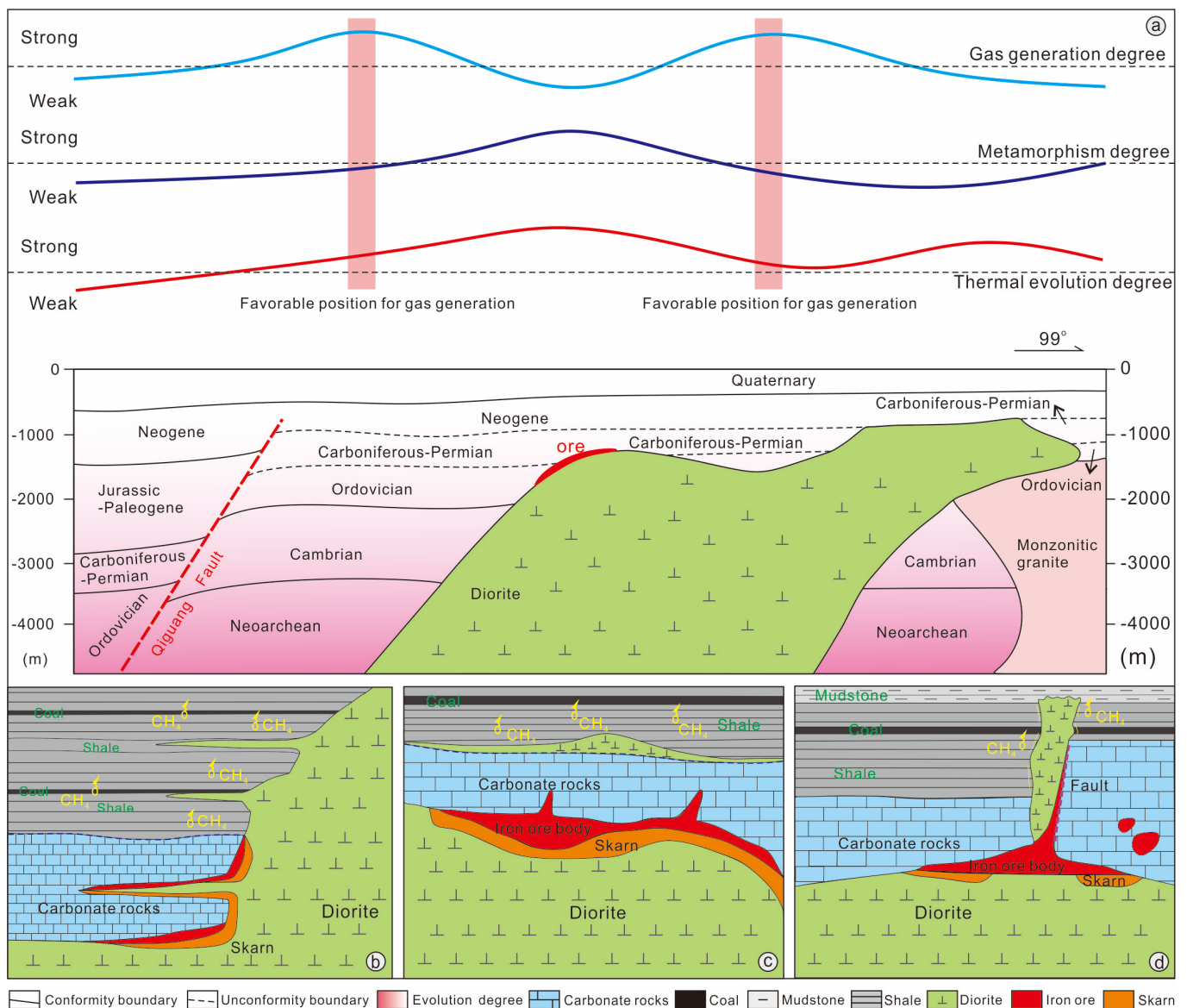


Figure 5. Mineralization and enrichment mechanism of multi-minerals. (a) Thermal evolution degree, metamorphism degree, gas generation degree, and magma intrude into Paleozoic strata and iron ore enrichment areas. (b) The magma invades the shale layer along the rock layer. (c) The laccolith type invades the stratum. (d) The dike type invades the stratum.

4. Mineralization Regularity of Skarn-Type Iron Ore

The genesis of skarn-type iron ore involves an intricate and protracted geological process, typically characterized by complexity and multiple stages of formation [59]. Varied metallogenic environments and mechanisms suggest differences in mineral sources and enrichment methods. The spatial distribution of rock mass in the HHBC is inferred from geophysical data and a limited number of boreholes. The intrusion predominantly occurs in the lower part of the Ordovician and Carboniferous, with the uppermost intrusion layer situated in the upper part of the Permian. The Taiyuan and Shanxi Formations of the Carboniferous–Permian are commonly invaded, and contact metasomatic iron bodies are predominantly located in the contact zone between the Carboniferous–Permian coal measures and magmatic rocks (Figure 5b). Considering the published ages of the skarn-type deposits and ore-forming rocks in the eastern part of the NCC, the U-Pb ages of diorite in ore-forming geologic bodies are (131.6 ± 1.7) Ma and (130.0 ± 2.3) Ma [34,60–62]. This period coincided with the peak of the lithosphere thinning of the NCC [63], signifying that

the extensive skarn-type iron mineralization in North China is a response to and product of the lithosphere thinning and destruction of the NCC.

Previous research has established that the HHBC iron deposit originates from hydrothermal metasomatism, involving the infiltration and filling of the ore-forming fluid within suitable iron-enriched sites in the rock mass and carbonate strata after the magma intrusion rock forming [64]. From the rock mass to the stratum direction, the structural planes exhibit distinct metallogenic belt and alteration characteristics, broadly classified into three lithofacies belts based on the magmatic rock-ore body-surrounding rock [65]. The primary zoning includes fresh diorite, altered diorite, internal skarn, mineralized skarn, ore body, external skarn, marble, and limestone. Notably, the iron ore in the study area predominantly formed during the degradation and alteration stage of skarn. Examining alteration characteristics, unaltered rocks in the study area typically display the characteristics of dark mineral enrichment and high magnetic susceptibility. In the intrusive rocks near sodium metasomatic alteration, the dark mineral content is minimal, with the metallogenic material primarily derived from Fe-rich magmatic fluid [66]. This suggests that during the albite alteration process of the diorite body within the carbonate formation, high-temperature hydrothermal fluid disintegrates and eliminates dark minerals and magnetite in the rock mass, converting iron into iron-bearing hydrothermal fluid. Throughout the mineralization process, carbonate strata and gypsum strata contribute a significant number of Na^+ , Cl^- , F^- , H^+ , $+\text{CO}_2^{2-}$, and SO_4^{2-} ions as mineralizers [16,67,68] and form iron deposits [59]. The intricate interplay of alteration processes and mineralization conditions in the study area underscores the multifaceted nature of skarn-type iron ore formation.

5. The Relationship between NCC Destruction and the Mineralization of Skarn-Type Iron Ore, CBM, and Shale Gas

The North China Craton is an important skarn-type iron ore metallogenic province and one of the significant iron ore-rich areas in China. From east to west, the metallogenic area can be roughly divided into two metallogenic belts: the East iron metallogenic belt, located on the west side of the Tanlu fault zone, represented by iron ore deposits in the Jinan–Laiwu area; and the West iron metallogenic belt, located in the middle of the NCC, represented by the Handan–Xingtai iron ore deposit. A large number of high-precision isotopic chronology data show that skarn-type iron ores in eastern China were mostly formed at ~130 Ma and have concentrated explosive metallogenic characteristics [65,66,68].

The iron ore in the HHBC is mainly produced in the Dazhang–Litun–Pandian area, and it belongs to a typical skarn-type iron ore deposit that is part of the Ji'nan–Laiwu iron ore deposit. The age of ore formation is consistent with the emplacement time of the diorite body. Zircon U-Pb chronology indicates that the geological body responsible for ore formation in the Dazhang–Litun–Pandian area corresponds to mid-basic intrusive rock formed during the late Mesozoic (130–131 Ma), which aligns with the peak period of lithosphere thinning and destruction in the NCC. This reflects the close genetic relationship between large-scale mineralization and NCC destruction, and plays a crucial role in the extensive mineralization of the HHBC [69,70]. CBM and shale gas are primarily concentrated in the Zhaoguan and Changqing areas, which are important regions known for their abundant gas resources within this research area. The ore-forming geological bodies are Carboniferous–Permian coal measures (coal seams and shale). It can be seen that the characteristics of mineral output and distribution are closely related to the distribution of magma intrusion. The main production of iron ore occurs in the contact zone between the rock mass and surrounding carbonate rocks, with varying distances from the ore body, resulting in a variety of mineralization modes for iron ore (Figure 5b–d). The iron ore belt is closely associated with intrusive bodies and is enriched along the rock strata. The gas enrichment zone is influenced by the location and mode of magma intrusion, with enrichment intensity inversely proportional to the distance from the intrusion (Figure 6).

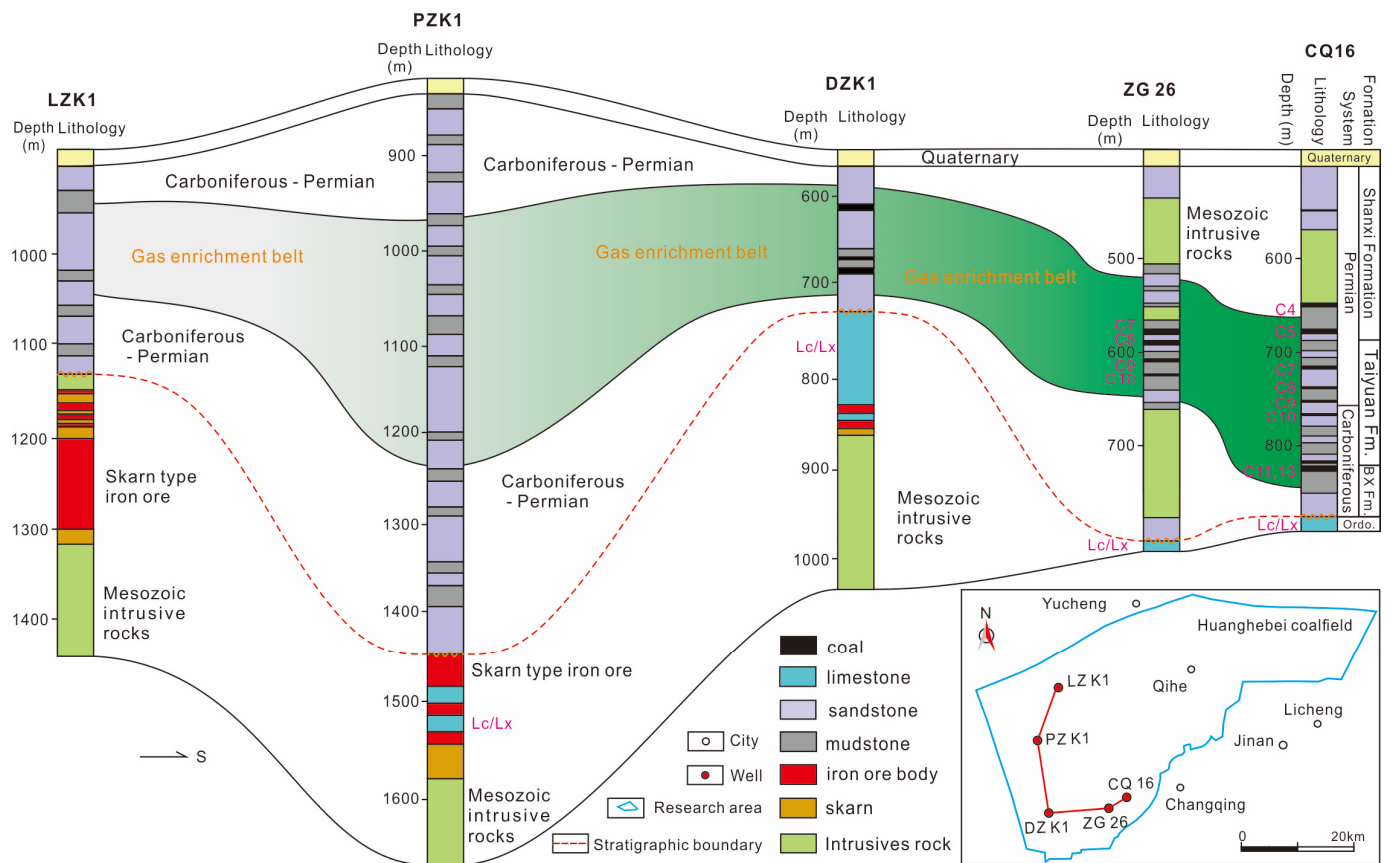


Figure 6. Distribution characteristics of iron ore belt, CBM, and shale gas belt in Paleozoic coal measures. Abbreviations: Ordo = Ordovician, Fm. = Formation, BX = Benxi, C5 = No. 5 coal seam, Lx = xujiazhuang limestone, Lc = caobugou limestone.

In the Early Cretaceous, subduction, rotation, retreat, and retreat of the Paleo–Pacific plate, as well as its retention in the mantle transition zone, caused the unsteady flow beneath the East Asian continent. This resulted in strong metasomatism from deep melts and fluids in the eastern part of the NCC. The content of lithospheric mantle melts increased while the viscosity of the lithosphere decreased, forming a highly enriched lithospheric mantle [68] (Figure 7a). The interaction between the melts and fluids produced by partial melting of both the mantle and the lower crust may generate mineralization-friendly magma [69]. During the coupling period of the Paleo–Pacific subduction plate and the overlying lithospheric mantle, dehydration of the subduction plate weakened NCC’s mantle leading to rollback initiation for the Paleo–Pacific plate. The metasomatized cratonic lithospheric mantle was exposed to the laterally flowing asthenosphere mantle and was heated and melted, forming a magma rich in iron [71]. During this period, the addition of subducted oceanic crust materials led to the water-rich and oxidized characteristics of the lithospheric mantle [71–75]. Subsequently, crystallization and cooling occurred during the re-emplacment of mixed magma, resulting in the dissolution of iron-rich magmatic–hydrothermal fluid. The fluid interacted with marine carbonate rocks in the Paleozoic Ordovician Majiagou Formation contact zone [76], leading to the formation of skarn-type iron deposits in the NCC [12,23,69,77].

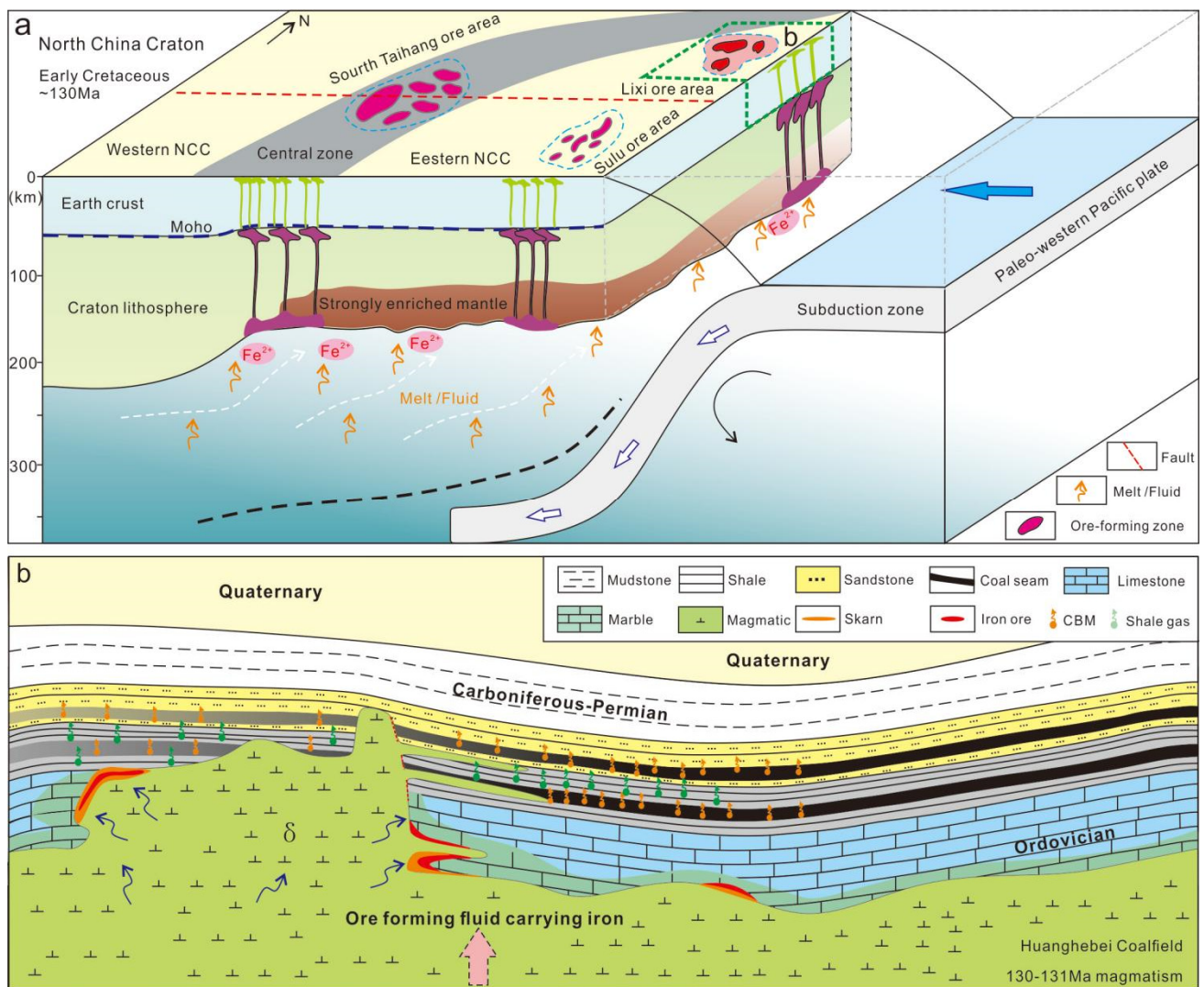


Figure 7. The relationship between NCC destruction and the mineralization of skarn-type iron ore, CBM, and shale gas. (a) Early Cretaceous deep magmatic intrusion process of the NCC and the relationship between destruction of the NCC and the mineralization mechanism of multi-minerals (modifies from [68]). (b) Magmatic intrusion and CBM-shale gas-iron ore metallogenic model.

The intrusion of magma brings a large number of heat sources, which significantly influences the thermal evolution process of organic matter in Paleozoic coal measures (Figure 7b). Due to the heat release from magma intrusion, the R^0_{max} (up to more than 5%) of organic matter in the surrounding rock of the study area increased sharply, surpassing the thermal evolution maturity level observed in sedimentary basins. This indicates that magma intrusion can accelerate the maturity of organic matter in the surrounding rock and promote hydrocarbon generation [78]. Various coal types with different degrees of metamorphism, and even abnormally high degrees, are formed, contributing to the varying production of coalbed methane (CBM) in coal. The thermal evolution degree of dispersed organic matter in shale has significantly increased, resulting in the formation of shale gas to varying extents [23]. As the distance between the magma and the contact surface (the contact part between the intrusion and the surrounding rock) decreases, there is a rapid decrease in the organic carbon content in the surrounding rock, a sharp decrease in R^0_{max} , and a gradual increase in hydrocarbon content in the surrounding rock. This suggests that the magma intrusion can effectively promote hydrocarbon generation [79–82].

In summary, the primary genesis mechanism for skarn-type iron deposits in the study area during the Yanshanian period is contact metasomatism of large-scale magmatic–

hydrothermal fluids. Simultaneously, this process serves as the predominant driving force behind the extensive enrichment of oil and gas, as well as mineralization in the Paleozoic coal measures. Despite variations in ore-forming parent materials, mineral types, and metallogenic mechanisms, the presence of age-inconsistent minerals establishes a regionally interconnected magmatic–hydrothermal metallogenic system. Building upon this research, the author contends that the multi-mineral metallogenic model proposed in this paper offers a fresh perspective for future investigations into hydrothermal deposits, presenting a novel direction for prospecting “coexistence in the same basin” minerals.

6. Conclusions

1. Various stages of magmatic intrusion during the Yanshanian period significantly influenced the Late Paleozoic coal measures in the HHBC. The coal measures exhibit distinct ranks, ranging from medium-rank bituminous C to A and high-rank anthracite C, resulting in noticeable differences in gas generation among different coal ranks. The shale between the coal seams C5 and C7 emerges as excellent, with a good hydrocarbon-generating capacity during the middle-maturity stage.
2. The “Intrusion along the rock layer type” proves most conducive to shale gas enrichment, while the “laccolith type” is more favorable for shale gas enrichment compared to “dike type” intrusions, which have a limited impact on shale gas enrichment.
3. The mineralization process of CBM, shale gas, and iron ore is influenced by Yanshanian-period magma. The enrichment degree of CBM and shale gas exhibits an inverse correlation with the distance from the magmatic intrusion. Iron deposits demonstrate a close association with the magmatic intrusion, with enhanced enrichment along the rock layer.

Author Contributions: L.Y. and D.W. proposed the main academic ideas of the manuscript and participated in directing the writing of the entire manuscript. L.Y., D.W., H.W., Y.L., H.L., Y.Z., L.S. and Z.L. were mainly responsible for data collection and processing and completed the writing of the paper. All authors contributed to the interpretation of the data and the final manuscript. All authors have read and agreed to the published version of the manuscript.

Funding: This study was co-funded by the National Natural Science Foundation of China (42372132), the Hebei Province Resources Survey Research Laboratory Open Fund Project, the Shandong Institute of Coal Geology Planning and Investigation Open Fund Project (SDMTKCY-2022-02), the Green cooperative exploration innovation team of coal, iron and gas in coal basin, Shandong Coalfield Geology Bureau.

Data Availability Statement: Data are contained within the article.

Acknowledgments: I would like to thank the Shandong Coal Geology Planning and Survey Institute for its support in sampling, testing, and data processing, and the reviewers for their hard work.

Conflicts of Interest: The authors declare no conflicts of interest.

References

1. Zhai, M.G. Tectonic evolution of the North China Craton. *J. Geomech.* **2019**, *25*, 722–745.
2. Zhu, R.X.; Yang, J.H.; Wu, F.Y. Timing of destruction of the North China Craton. *Lithos* **2012**, *149*, 51–60. [[CrossRef](#)]
3. Li, S.Z.; Suo, Y.H.; Li, X.Y.; Zh, J.; Santosh, M.; Wang, P.C.; Wang, G.Z.; Guo, L.L.; Yu, S.Y.; Lan, H.Y.; et al. Mesozoic tectono-magmatic response in the East Asian ocean-continent connection zone to subduction of the Paleo-Pacific Plate. *Earth-Sci. Rev.* **2019**, *192*, 91–137. [[CrossRef](#)]
4. Zhu, R.X.; Xu, Y.G.; Zhu, G.; Zhang, H.F.; Xia, Q.K.; Zheng, T.Y. Destruction of the North China Craton. *Sci. China Earth Sci.* **2012**, *55*, 1565–1587. (In Chinese) [[CrossRef](#)]
5. Dong, Y.P.; Sun, S.S.; Santosh, M.; Zhao, J.; Sun, J.P.; He, D.F.; Shi, X.; Hui, B.; Cheng, C.; Zhang, G.W. Central China Orogenic Belt and amalgamation of East Asian continents. *Gondwana Res.* **2021**, *100*, 131–194.
6. Mao, J.W.; Pirajno, F.; Xiang, J.F.; Gao, J.J.; Ye, H.S.; Li, Y.F.; Guo, B.J. Mesozoic molybdenum deposits in the east Qinling-Dabie orogenic belt: Characteristics and tectonic settings. *Ore Geol. Rev.* **2011**, *43*, 264–293. [[CrossRef](#)]
7. Wang, H.H.; Shen, L.J.; Wang, D.D.; Zhu, Y.Z.; Li, Z.X.; Wang, Y.J.; Mao, Q. Study on Mesozoic magmatic intrusion and Paleozoic multi-mineral genesis mechanism in Huanghebei Coalfield, Shandong Province. *Coal Geol. Explor.* **2021**, *49*, 83–92. (In Chinese)
8. Einaudi, M.T. *Skarn Deposits*; Economic Geology Publishing Company: Littleton, CO, USA, 1981; Volume 75, pp. 317–391.

9. Meinert, L.D. Mineralogy and petrology of iron skarns in western British Columbia, Canada. *Econ. Geol.* **1984**, *79*, 869–882. [[CrossRef](#)]
10. Meinert, L.D.; Dipple, G.M.; Nicolescu, S. World skarn deposits. *Econ. Geol. 100th Anniv.* **2005**, 299–336. [[CrossRef](#)]
11. Wang, D.D.; Zhang, G.C.; Li, Z.X.; Dong, G.Q.; Sun, R.; Guo, S.; Wu, Y. The Development Characteristics and Distribution Predictions of the Paleogene Coal-measure Source Rock in the Qiongdongnan Basin, Northern South China Sea. *Acta Geol. Sin. Engl. Ed.* **2021**, *95*, 105–120. [[CrossRef](#)]
12. Qi, P.; Yin, Y.T.; Jin, S.; Wei, W.B.; Xu, L.Y.; Dong, H.; Huang, J.H. Three-Dimensional audio-magnetotelluric imaging including surface topography of the cimabanshuo porphyry copper deposit, Tibet. *Minerals* **2021**, *11*, 1424. [[CrossRef](#)]
13. Zhao, X.F.; Li, Z.K.; Zhao, S.R.; Bi, S.J.; Li, J.W. Early Cretaceous Regional-Scale Magmatic-Hydrothermal Metallogenic System at the Southern Margin of the North China Craton. *Earth Sci.* **2019**, *44*, 52–68. (In Chinese)
14. Blakey, R. Mollewide Plate Tectonic Maps, Colorado Plateau Geosystems. World Wide Web Address. Available online: <http://cpgeosystems.com/mollglobe.html> (accessed on 11 February 2023).
15. Dong, Y.; Santosh, M. Tectonic architecture and multiple orogeny of the Qinling Orogenic Belt, Central China. *Gondwana Res.* **2016**, *29*, 1–40. [[CrossRef](#)]
16. Wen, G.; Bi, S.J.; Li, J.W. Role of evaporitic sulfates in iron skarn mineralization: A fluid inclusion and sulfur isotope study from the Xishimen deposit, Handan-Xingtai district, North China Craton. *Miner. Depos.* **2017**, *52*, 495–514. [[CrossRef](#)]
17. Wang, H.H.; Zhang, H.; Gong, G.; Zhang, Z.M. Coalfield Geological Features and Contemporary Coalfield Partitioning in Shandong Province. *Coal Geol. China* **2017**, *29*, 18–22+30. (In Chinese)
18. Zhou, M.L.; Yin, L.S.; Shao, Y.B.; Wang, H.H.; Zhang, X.B.; Wu, Y.; Wang, D.D. The Enrichment Conditions and Resource Potential of Marine-Continental Transitional Coal-Measure Shale Gas: A Case Study of the Permo-Carboniferous System in the Huanghebei Coalfield of North China. *Glob. J. Earth Sci. Eng.* **2020**, *7*, 22–36. [[CrossRef](#)]
19. Chen, B.; Zhai, M.G.; Tian, W. Origin of the Mesozoic magmatism in the North China Craton: Constraints from petrological and geochemical data. *Geol. Soc. Spec. Publ.* **2007**, *280*, 131–151. [[CrossRef](#)]
20. Chen, B.; Tian, W.; Jahn, B.M.; Chen, Z.C. Zircon SHRIMP U-Pb ages and in-situ Hf isotopic analysis for the Mesozoic intrusions in South Taihang, North China craton: Evidence for hybridization between mantle-derived magmas and crustal components. *Lithosphere* **2008**, *102*, 118–137. [[CrossRef](#)]
21. Li, J.W.; Zhao, X.F.; Zhou, M.F.; Ma, C.Q.; de Souza, Z.S.; Vasconcelos, P. Late Mesozoic magmatism from the Daye region, eastern China: U-Pb ages, petrogenesis, and geodynamic implications. *Contrib. Mineral. Petrol.* **2009**, *157*, 383–409. [[CrossRef](#)]
22. Dong, Y.; Liu, X.F.; Jiang, H.D.; Li, C.H.; Yi, L.W.; Zou, J.X.; Huang, Y.P. Genesis and metallogenic significance of the Indosinian intermediate-acidic intrusive rocks in the west porphyry belt, Zhongdian island arc, Yunnan. *Geol. China* **2012**, *39*, 887–899. (In Chinese)
23. Yin, L.S.; Wang, D.D.; Sun, L.J.; Zhu, Z.Y.; Li, Z.X.; Wang, Y.J. Coexistence and Development Model of Multi-Minerals Dominated by Multilayer Magma Intrusion: A Case Study of Huanghebei Coalfield in North China Basin. *Glob. J. Earth Sci. Eng.* **2021**, *8*, 45–61.
24. Scotese, C.R. *Atlas of Early Cretaceous Paleogeographic Maps, PALEOMAP Atlas for ArcGIS, Volume 2, The Cretaceous, Maps 23–31, Mollweide Projection*; PALEOMAP Project: Evanston, IL, USA, 2014.
25. Ying, J.; Zhang, H.; Tang, Y. Crust-mantle interaction in the central North China Craton during the Mesozoic: Evidence from zircon U-Pb chronology, Hf isotope and geochemistry of syenitic-monzonitic intrusions from Shanxi province. *Lithos* **2011**, *125*, 449–462. [[CrossRef](#)]
26. Zhao, G.C.; Cawood, P.A.; Li, S.Z.; Wilde, S.A.; Sun, M.; Zhang, J.; He, Y.H.; Yin, C.Q. Amalgamation of the North China Craton: Key Issues and Discussion. *Precambrian. Res.* **2012**, 222–223, 55–76. [[CrossRef](#)]
27. ECE. *International Codification System for Medium and High Rank Coals*; Erdol & Kohle Erdgas Petrochemie: Geneva, Switzerland, 1988.
28. Li, X.; Zhou, J.; Jiao, L.; Sun, B.; Huang, Y.; Huang, D.; Zhang, J.; Shao, L. Coalbed Methane Enrichment Regularity and Model in the Xishanyao Formation in the Santanghu Basin, NW China. *Minerals* **2023**, *13*, 1369. [[CrossRef](#)]
29. Yuan, Y.; Shan, Y.S.; Tang, Y.; Cao, D.Y. Coalbed Methane Enrichment Regularity and Major Control Factors in the Xishanyao Formation in the Western Part of the Southern Junggar Basin. *Acta Geol. Sin. Engl. Ed.* **2020**, *94*, 485–500. [[CrossRef](#)]
30. Kaiser, W.R.; Hamilton, D.S.; Scott, A.R. Geological and hydrological controls on the producibility of coalbed methane. *J. Geol. Soc.* **1994**, *151*, 417–420. [[CrossRef](#)]
31. Moore, T.A. Coalbed methane: A review. *Int. J. Coal Geol.* **2012**, *101*, 36–81. [[CrossRef](#)]
32. Zhang, Z.; Qin, Y.; Zhuang, X.G.; Li, G.Q.; Liu, D.H. Geological controls on the CBM productivity of No.15 coal seam of Carboniferous–Permian Taiyuan Formation in southern Qinshui Basin and prediction for CBM high-yield potential regions. *Acta Geol. Sin. Engl. Ed.* **2018**, *92*, 2310–2332.
33. Lamarre, R. Coalbed Methane Production from Ferron Coals in East-Central Utah1. *Mt. Geol.* **2006**, *43*, 207–211.
34. Li, J.W.; Vasconcelos, P.M.; Zhou, M.F.; Deng, X.D.; Cohen, B.; Bi, S.J.; Zhao, X.F.; Selby, D. Longevity of magmatic-hydrothermal systems in the Daye Cu-Fe-Au District, eastern China with implications for mineral exploration. *Ore Geol. Rev.* **2014**, *57*, 375–392. [[CrossRef](#)]
35. Chen, Y.; Tang, D.; Xu, H.; Li, Y.; Meng, Y. Structural controls on coalbed methane accumulation and high production models in the eastern margin of Ordos Basin, China. *J. Nat. Gas Sci. Eng.* **2015**, *23*, 524–537. [[CrossRef](#)]

36. Jia, T.; Zhang, Z.; Wei, G. Mechanism of stepwise tectonic control on gas occurrence: A study in North China. *Int. J. Min. Sci. Technol.* **2015**, *25*, 601–606. [[CrossRef](#)]
37. Tao, S.; Tang, D.; Xu, H.; Gao, L.; Fang, Y. Factors controlling high-yield coalbed methane vertical wells in the Fanzhuang Block, Southern Qinshui Basin. *Int. J. Coal Geol.* **2014**, *134*, 38–45. [[CrossRef](#)]
38. Yao, Y.B.; Liu, D.M.; Yan, T.T. Geological and hydrological controls on the accumulation of coalbed methane in the weibe field, southeastern ordos basin. *Int. J. Coal Geol.* **2014**, *121*, 148–159. [[CrossRef](#)]
39. Jia, J.; Wang, D.; Li, B.; Wu, Y.; Zhao, D. Molecular simulation study on the effect of coal metamorphism on the competitive adsorption of CO₂/CH₄ in binary system. *Fuel* **2023**, *335*, 127046. [[CrossRef](#)]
40. Bishop, A.N.; Abbott, G.D. The interrelationship of biological marker maturity parameters and molecular yields during contact metamorphism. *Geochim. Cosmochim. Acta* **1993**, *57*, 3661–3668. [[CrossRef](#)]
41. Bishop, A.N.; Abbott, G.D. Vitrinite reflectance and molecular geochemistry of Jurassic sediments: The influence of heating by Tertiary dykes (northwest Scotland). *Org. Geochem.* **1995**, *22*, 165–177. [[CrossRef](#)]
42. Groshong, R.H.; Pashin, J.C.; McIntyre, M.R. Structural controls on fractured coal reservoirs in the southern Appalachian Black Warrior foreland basin. *J. Struct. Geol.* **2009**, *31*, 874–886. [[CrossRef](#)]
43. Liu, D.N.; Zhang, Y.; Zhou, A.; Nnachi, E.N.; Huo, S.; Zhang, Q. The Kaolinite Crystallinity and Influence Factors of Coal-Measure Kaolinite Rock from Datong Coalfield, China. *Minerals* **2022**, *12*, 54. [[CrossRef](#)]
44. Sun, R.; Li, Z.; Zhao, Z.; Yang, H.Z.; Wang, X.Y.; Zhao, Z. Characteristics and origin of the Lower Oligocene marine source rocks controlled by terrigenous organic matter supply in the Baiyun Sag, northern South China Sea. *J. Pet. Sci. Eng.* **2020**, *187*, 106821. [[CrossRef](#)]
45. Li, L.; Liu, Z.; Jiang, L.; George, S.C. Organic petrology and geochemistry of Lower Cretaceous lacustrine sediments in the Chaoyang Basin (Liaoning Province, northeast China): Influence of volcanic ash on algal productivity and oil shale formation. *Int. J. Coal Geol.* **2021**, *233*, 103653. [[CrossRef](#)]
46. Das, R.; Zhang, Y.; Schaub, P.; Cleary, P.W. Modelling rock fracturing caused by magma intrusion using the smoothed particle hydrodynamics method. *Comput. Geosci.* **2014**, *18*, 927–947. [[CrossRef](#)]
47. Zhang, W.; Wang, Q.; Ye, J.; Zhou, J. Fracture development and fluid pathways in shales during granite intrusion. *Int. J. Coal Geol.* **2017**, *183*, 25–37. [[CrossRef](#)]
48. Stagpoole, V.; Funnell, R. Arc magmatism and hydrocarbon generation in the northern Taranaki Basin, New Zealand. *Pet. Geosci.* **2001**, *7*, 255–267. [[CrossRef](#)]
49. Agirrezabala, L.M.; Permanyer, A.; Suarez-Ruiz, I.; Dorronsoro, C. Contact metamorphism of organic-rich mudstones and carbon release around a magmatic sill in the Basque-Cantabrian Basin, western Pyrenees. *Org. Geochem.* **2014**, *69*, 26–35. [[CrossRef](#)]
50. Li, X.; Wang, Q.; Zhang, W.; Yin, H. Contact metamorphism of shales intruded by a granite dike: Implications for shale gas preservation. *Int. J. Coal Geol.* **2016**, *159*, 96–106. [[CrossRef](#)]
51. Arora, A.; Dutta, S.; Gogoi, B.; Banerjee, S. The effects of igneous dike intrusion on organic geochemistry of black shale and its implications: Late Jurassic Jhuran Formation, India. *Int. J. Coal Geol.* **2017**, *178*, 84–99. [[CrossRef](#)]
52. Misra, S.; Varma, A.K.; Das, S.K.; Mani, D.; Biswas, S. Thermal controls of lamprophyre sill on hydrocarbon generation outlook of shale beds in Raniganj basin, India. *J. Nat. Gas Sci. Eng.* **2018**, *56*, 536–548. [[CrossRef](#)]
53. Rahman, M.W.; Rimmer, S.M.; Rowe, H.D. The impact of rapid heating by intrusion on the geochemistry and petrography of coals and organic-rich shales in the Illinois Basin. *Int. J. Coal Geol.* **2018**, *187*, 45–53. [[CrossRef](#)]
54. Wan, C.; Li, J.; Jin, Q.; Zhao, Y.; Yang, Z. Magma intrusion and its effects on enrichment of shale gas in fault subsidence basin. *Nat. Gas Geosci.* **2011**, *22*, 1088–1092. (In Chinese)
55. Deng, Z.C. Direct dating of hydrothermal tungsten mineralization using in situ wolframite U-Pb chronology by laser ablation ICP-MS. *Chem. Geol.* **2019**, *515*, 94–104. [[CrossRef](#)]
56. Svensen, H.; Planke, S.; Malthe-Sørenssen, A.; Jamtveit, B.; Myklebust, R.; Rasmussen Eidem, T.; Rey, S.S. Release of methane from a volcanic basin as a mechanism for initial Eocene global warming. *Nature* **2004**, *429*, 542–545. [[CrossRef](#)] [[PubMed](#)]
57. Aarnes, I.; Svensen, H.; Connolly, J.A.; Podladchikov, Y.Y. How contact metamorphism can trigger global climate changes: Modeling gas generation around igneous sills in sedimentary basins. *Geochim. Cosmochim. Acta* **2010**, *74*, 7179–7195. [[CrossRef](#)]
58. Aarnes, I.; Frisstad, K.; Planke, S.; Svensen, H. The impact of host-rock composition on devolatilization of sedimentary rocks during contact metamorphism around mafic sheet intrusions. *Geochim. Geophys. Geosystems.* **2011**, *12*. [[CrossRef](#)]
59. Chen, Y.; Zhang, Z.C. Study on Source, Transport and the Enrichment Mechanism of Iron in Iron Skarn Deposits. *Rock Ore Test.* **2012**, *31*, 889–897.
60. Deng, X.D.; Li, J.W.; Wen, G. Dating iron skarn mineralization using hydrothermal allanite-(La) U-Th-Pb isotopes by laser ablation ICP-MS. *Chem. Geol.* **2014**, *382*, 95–110. [[CrossRef](#)]
61. Deng, X.D.; Li, J.W.; Wen, G. U-Pb Geochronology of Hydrothermal Zircons from the Early Cretaceous Iron Skarn Deposits in the Handan-Xingtai District, North China Craton. *Econ. Geol.* **2015**, *110*, 2159–2180. [[CrossRef](#)]
62. Deng, X.D.; Li, J.W.; Luo, T.; Wang, H.Q. Dating magmatic and hydrothermal processes using andradite-rich garnet U-Pb geochronometry. *Contrib. Mineral. Petrol.* **2017**, *172*, 71. [[CrossRef](#)]
63. Zhai, M.G. Tectonic evolution and metallogenesis of North China Craton. *Miner. Depos.* **2010**, *29*, 24–36. (In Chinese)
64. Xu, J.Q.; Li, Z.; Shi, Y.H. Jurassic detrital zircon U-Pb and Hf isotopic geochronology of Luxi Uplift, eastern North China, and its provenance implications for tectonic-paleogeographic reconstruction. *J. Asian Earth Sci.* **2013**, *78*, 184–197. [[CrossRef](#)]

65. Bowman, J.R. Stable-isotope systematic of skarns. In *Mineralized Intrusion-Related Skarn System*; Lentz, D.R., Ed.; Mineral Association of Canada Short Course Series; Mineralogical Association of Canada: Ottawa, ON, Canada, 1998; pp. 99–145.
66. Jin, Z.; Zhang, Z.; Santosh, M.; Han, L. Occurrence and Chemical Compositions of Amphiboles in Altered Dioritic Rocks of Laiwu Skarn-Type Iron Deposit in West Shandong Area, China. *Resour. Geol.* **2018**, *68*, 425–445. [[CrossRef](#)]
67. Xie, G.Q.; Mao, J.W.; Zhu, Q.Q.; Yao, L.; Li, Y.H.; Li, W.; Zhao, H.J. Geochemical constraints on Cu-Fe and Fe skarn deposits in the Edong district, Middle-Lower Yangtze River metallogenic belt, China. *Ore Geol. Rev.* **2015**, *64*, 425–444. [[CrossRef](#)]
68. Zhu, R.X.; Fan, H.R.; Li, J.W.; Meng, Q.R.; Li, S.R.; Zeng, Q.D. Decratonic gold deposits. *Sci. China Earth Sci.* **2015**, *58*, 1523–1537. (In Chinese) [[CrossRef](#)]
69. Duan, Z. The Mineralization and Mechanism of the Iron Skarn Deposits in Laiwu District, Shandong Province. Ph.D. Thesis, China University of Geosciences, Wuhan, China, 2020. (In Chinese)
70. Seton, M.; Müller, R.D.; Zahirovic, S.; Gaina, C.; Torsvik, T.; Shephard, G.; Talsma, A.; Gurnis, M.; Turner, M.; Maus, S.; et al. Global continental and ocean basin reconstructions since 200 Ma. *Earth Sci. Rev.* **2012**, *113*, 212–270. [[CrossRef](#)]
71. Richards, J.P. Magmatic to hydrothermal metal fluxes in convergent and collided margins. *Ore Geol. Rev.* **2011**, *40*, 1–26. [[CrossRef](#)]
72. Richards, J.P. Postsubduction porphyry Cu-Au and epithermal Au deposits: Products of remelting of subduction-modified lithosphere. *Geology* **2009**, *37*, 247–250. [[CrossRef](#)]
73. Lee, J.Y.; Marti, K.; Severinghaus, J.P.; Kawamura, K.; Yoo, H.S.; Lee, J.B.; Kim, J.S. A redetermination of the isotopic abundances of atmospheric Ar. *Geochim. Cosmochim. Acta* **2006**, *70*, 4507–4512. [[CrossRef](#)]
74. Wang, R.; Richards, J.P.; Hou, Z.Q.; Yang, Z.M. Extent of underthrusting of the Indian plate beneath Tibet controlled the distribution of Miocene porphyry Cu-Mo ± Au deposits. *Miner. Depos.* **2014**, *49*, 165–173. [[CrossRef](#)]
75. Wang, R.; Richards, J.P.; Hou, Z.; Yang, Z.; DuFrane, S.A. Increased magmatic water content—the key to Oligo-Miocene porphyry Cu-Mo ± Au formation in the eastern Gangdese belt, Tibet. *Econ. Geol.* **2014**, *109*, 1315–1339. [[CrossRef](#)]
76. Zhang, Z.C.; Hou, T.; Li, H.M.; Li, J.W.; Zhang, Z.H.; Song, X.Y. Enrichment mechanism of iron in magmatic-hydrothermal system. *Acta Petrol. Sin.* **2014**, *30*, 1189–1204. (In Chinese)
77. Ju, N.; Ren, Y.S.; Zhang, S.; Bi, Z.W.; Shi, L.; Zhang, D.; Wu, T. Metallogenic Epoch and Tectonic Setting of Saima Niobium Deposit in Fengcheng, Liaoning Province, NE China. *Minerals* **2019**, *9*, 80. [[CrossRef](#)]
78. Monreal, F.R.; Villar, H.J.; Baudino, R.; Delpino, D.; Zencich, S. Modeling an atypical petroleum system: A case study of hydrocarbon generation, migration and accumulation related to igneous intrusions in the Neuquen Basin, Argentina. *Mar. Pet. Geol.* **2009**, *26*, 590–605. [[CrossRef](#)]
79. Fjeldskaar, W.; Helset, H.M.; Johansen, H.; Grunnaleite, I.; Horstad, I. Thermal modelling of magmatic intrusions in the Gjallar Ridge, Norwegian Sea: Implications for vitrinite reflectance and hydrocarbon maturation. *Basin Res.* **2008**, *20*, 143–159. [[CrossRef](#)]
80. Barker, C.E.; Bone, Y.; Lewan, M.D. Fluid inclusion and vitrinite-reflectance geothermometry compared to heat-flow models of maximum paleotemperature next to dikes, western onshore Gippsland Basin, Australia. *Int. J. Coal Geol.* **1998**, *92*, 27–42. [[CrossRef](#)]
81. Dow, W.G. Kerogen studies and geological interpretations. *J. Geochem. Explor.* **1977**, *47*, 435–510. [[CrossRef](#)]
82. George, S.C. Effect of igneous intrusion on the organic geochemistry of a siltstone and an oil shale horizon in the Midland Valley of Scotland. *Org. Geochem.* **1992**, *14*, 47–82. [[CrossRef](#)]

Disclaimer/Publisher’s Note: The statements, opinions and data contained in all publications are solely those of the individual author(s) and contributor(s) and not of MDPI and/or the editor(s). MDPI and/or the editor(s) disclaim responsibility for any injury to people or property resulting from any ideas, methods, instructions or products referred to in the content.